AGU
ADVANCING EARTH AND SPACE SCIENCE

Geophysical Research Letters®

Key Points:
- We present holographic measurements of droplet size, velocity, and acceleration from breaking waves in a turbulent wind wave experiment
- Droplet speed distributions are found to be skewed normal both in the horizontal and vertical directions
- Vertical acceleration distributions are found to be skewed normal while horizontal distributions follow previously proposed functional shape

Author Contributions:
Conceptualization: M. A. Erinin, B. Néel, D. J. Ruth, M. Mazzatenta, F. Veron, L. Deike
Data curation: M. A. Erinin, D. J. Ruth, M. Mazzatenta, R. D. Jaquette
Formal analysis: M. A. Erinin, L. Deike
Funding acquisition: F. Veron, L. Deike
Investigation: M. A. Erinin, B. Néel, D. J. Ruth, M. Mazzatenta, R. D. Jaquette
Methodology: M. A. Erinin
Software: M. A. Erinin
Writing – original draft: M. A. Erinin, L. Deike
Writing – review & editing: M. A. Erinin, B. Néel, D. J. Ruth, M. Mazzatenta, R. D. Jaquette, F. Veron, L. Deike

Speed and Acceleration of Droplets Generated by Breaking Wind-Forced Waves

M. A. Erinin[1] , **B. Néel[1]** , **D. J. Ruth[1]** , **M. Mazzatenta[1]** , **R. D. Jaquette[2]** , **F. Veron[2]** , and **L. Deike[1,3]**

[1]Department of Mechanical and Aerospace Engineering, Princeton University, Princeton, NJ, USA, [2]School of Marine Science and Policy, University of Delaware, Newark, DE, USA, [3]High Meadows Environmental Institute, Princeton University, Princeton, NJ, USA

Abstract Laboratory measurements of droplet size, velocity, and accelerations generated by mechanically and wind-forced water breaking waves are reported. The wind free stream velocity is up to 12 m/s, leading to wave slopes from 0.15 to 0.35 at a fetch of 23 m. The ratio of wind free stream and wave phase speed ranges from 5.9 to 11.1, depending on the mechanical wave frequency. The droplet size distribution in all configurations can be represented by two power laws, $N(d) \propto d^{-1}$ for drops from 30 to 600 μm and $N(d) \propto d^{-4}$ above 600 μm. The horizontal and vertical droplet velocities appear correlated, with drops with slower horizontal speed more likely to move upward. The velocity and acceleration distributions are found to be asymmetric, with the velocity probability density functions (PDFs) being described by a normal-inverse-Gaussian distribution. The horizontal acceleration PDF are found to follow a shape close to the one predicted for small particles in homogeneous and isotropic turbulence, while the vertical distribution follows an asymmetric normal shape, showing that both acceleration components are controlled by different physical processes.

Plain Language Summary Spray droplets generated by wave breaking events, are known to enhance the exchange of mass, momentum, and energy between the ocean and the atmosphere and play a key role in tropical cyclone intensification. The speed and acceleration of droplets produced by wind-forced breaking waves are key components in developing accurate models of such processes. However, while droplet size distributions have been discussed in many previous experiments, data or knowledge on the droplet velocity and acceleration statistics, due to the difficulty of such measurements, is scarce. Here, we present wind speed, surface elevation, and droplet size, speed, and acceleration statistics generated by breaking waves forced by wind and mechanical wave maker, for a wide range of wave slope and wind speed, using a state of the art in-line holographic droplet measurement system.

1. Introduction

At moderate to high wind speed above the ocean surface, spray droplets are generated by wind-forced breaking waves. These droplets are transported in the atmospheric boundary layer where they influence the transfer of mass, momentum, and heat between the ocean and the atmosphere (Andreas, 1992; Mestayer & Lefauconnier, 1988; Mueller & Veron, 2014a, 2014b), contribute to the sensible heat flux (Andreas & Decosmo, 2002), and participate in the intensification of tropical cyclones (Sroka & Emanuel, 2021). The transport of spray droplets is thought to be highly dependent on ejection of initial conditions as well as the interactions between droplets and the turbulent air, which are controlled by the droplet size, velocity, and acceleration distributions. These statistics play a key role in our understanding and modeling of spray on air-sea interaction (Deike, 2022; Peng & Richter, 2017; Richter et al., 2019). However, while droplet size distributions have been reported in wind-generated breaking waves (see Veron et al. (2012); Mehta et al. (2019); Troitskaya et al. (2018); Bruch et al. (2021)) knowledge and data on droplet velocity and acceleration statistics remain elusive in part due to the difficulty in performing such measurements.

Spray droplets are generated by breaking waves through three processes: bubble bursting, wave breaking, and wind shearing at high speeds. Bubble bursting (reviewed by Veron (2015) and Deike (2022)) is thought to mostly generate small sea spray droplets, typically $d < 10$ μm (De Leeuw et al., 2011); while wave breaking and wind shearing are believed to produce larger droplets (Andreas et al., 2010; Monahan, 1986; Veron, 2015). The motion

of the air above breaking waves is a dynamic and transient phenomena, which is significantly modified by the breaking waves. As an example, Buckley et al. (2020) recently reported that air flow separation downstream of the wave crests increases with wind speed and wave slope. These airflow modifications are thought to have a significant impact on the droplet production in breaking waves and have previously been linked to surface features such as the significant wave height (Ovadnevaite et al., 2014), wave age (Laussac et al., 2018), and mean square slope (Bruch et al., 2021).

In the field, droplet size distributions relatively close to the surface have been reported at various wind speeds and heights above the water waves (De Leeuw, 1986; Reid et al., 2001; Smith et al., 1993). Wu et al. (1984) found that vertical distribution of droplets varies greatly with droplet size, and that droplet concentrations are distributed in longitudinal patches with frequency comparable to that of the peak waves. In laboratory experiments, Veron et al. (2012), Fairall et al. (2009) and Mehta et al. (2019) studied droplets generation by breaking waves at moderate to high wind speeds and found the drop size distribution to follow $N(d) \propto d^{-2}$–d^{-3} for drops below a few hundred microns and $N(d) \propto d^{-3}$–d^{-5} for larger drops. In the field, Lenain and Melville (2017) measured droplet size distributions using an aircraft at altitudes ranging from 30 to 800 m and found large droplets ($d \geq 40\,\mu m$) present at those altitudes. Spray generation by mechanically generated plunging breakers was studied by Erinin et al. (2019), and recent direct numerical simulations have discussed the droplet generation processes in breaking waves (Mostert et al., 2022; Wang et al., 2016), comparable to those from Veron et al. (2012) and Erinin et al. (2019). Tang et al. (2017) studied the transport of droplets generated by breaking waves while Richter et al. (2019) studied the turbulent transport of tracer particles using large eddy simulations in the vicinity of moving surface waves.

Of the few studies that have measured droplet dynamics in wind-generated wave experiments, Koga (1981) and Koga (1984) measured the vertical distribution and velocity of large droplets ($d > 810\,\mu m$) produced by breaking waves and found that the horizontal droplet movement is primarily determined by the wind, while vertical movement is determined by gravity. More recently, Ramirez de la Torre et al. (2022) experimentally studied drop speeds and accelerations for mechanically and wind generated breaking waves. A number of laboratory and numerical experiments have investigated the motion of passive and inertial particles in canonical flows such as homogeneous isotropic turbulence (Aliseda et al., 2002; Huck et al., 2018; Ireland et al., 2016; La Porta et al., 2001; Mora et al., 2021; Obligado et al., 2020; Pujara et al., 2019; Sumbekova et al., 2017; Variano & Cowen, 2013) and boundary layers (Berk & Coletti, 2020; Stelzenmuller et al., 2017). Brandt and Coletti (2022) offer an extensive review on particle-laden turbulence. La Porta et al. (2001) studied the acceleration of droplets in homogeneous isotropic turbulence using laboratory experiments and found that the probability density function (PDF) of the acceleration shows long stretched exponential shape. A functional shape for the acceleration PDFs was proposed in Mordant et al. (2004) who assumed the acceleration vector to be isotropic. Stelzenmuller et al. (2017) studied the accelerations of particles in a turbulent boundary layer using numerical and laboratory experiments and found asymmetric log-normal acceleration distributions near the wall and good agreement with the previously proposed log-normal model away from the wall.

In this paper, experimental measurements of droplet speed, accelerations, and diameters are reported for breaking wind waves. The waves are generated by a combination of mechanical and wind forcing for a broad range of conditions. Section 2 presents the experimental methods, §3 the drop size distribution, and §4 discusses the velocity and acceleration distributions. Concluding remarks are given in §5.

2. Experimental Setup

Experiments were performed at the University of Delaware's Air-Sea Interaction Laboratory wind wave tank (see Buckley et al. (2020) for more details on the facility). Figure 1a shows a schematic of the wind wave tank (42 m long, 1 m wide, and 1.25 m tall), which is filled with chlorinated tap water to a depth of $h = 0.71$ m. Wind waves were produced by a combination of mechanical and wind forcing. Waves are mechanically forced using a computer-controlled, vertically-oscillating, wedge-shaped wave maker, with a central frequency of f_m, (in the current experiments $f_m = 1.0$ and 1.8 Hz are used) and side-bands of $\Delta f = 0.05$ Hz, resulting in a weakly focusing wave packet. Wind is produced by a computer-controlled closed-loop wind tunnel with a channel height of 0.54 m above the mean water level. The wind speed, denoted by U_0 in this paper, was measured at a fetch of 23.0 m and 36 cm above the mean water level using a pitot tube (pressure transducer Setra, Model: 264, 1" WC) recording
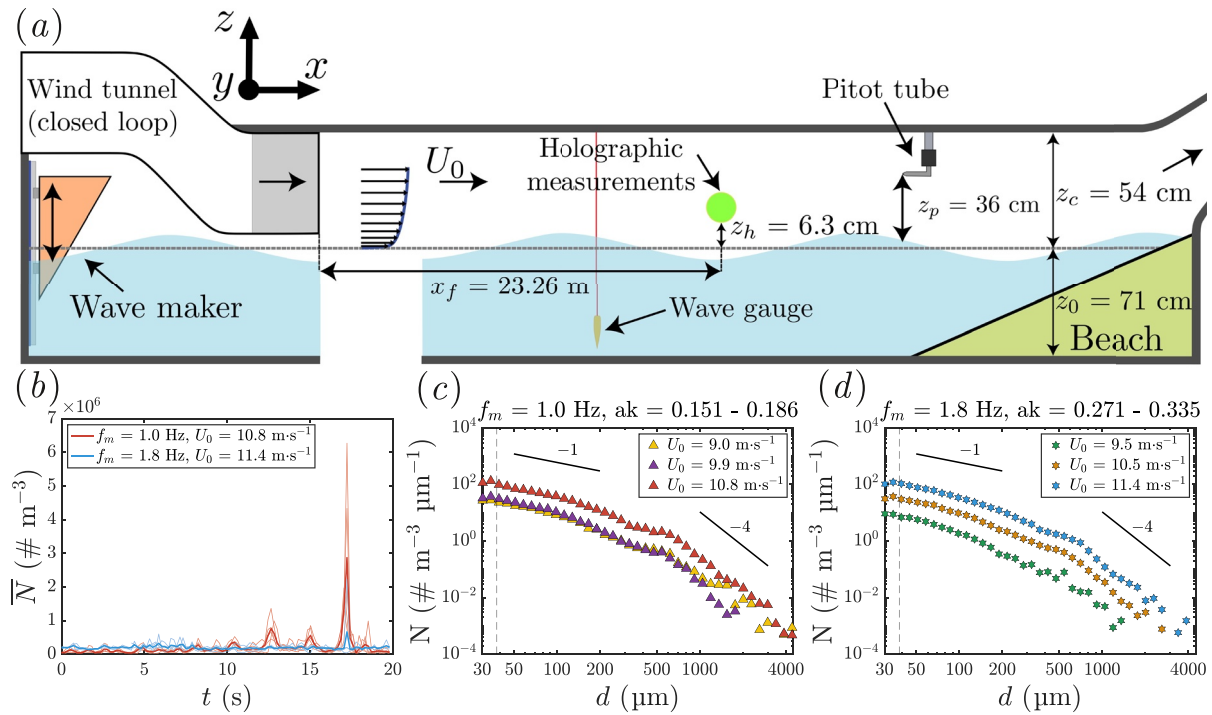
Figure 1. (a) Schematic of the wave tank, holographic droplet measurement system, wave gauge, and pitot tube. (b) Shows $N(t)$ ensemble averaged over multiple 20 s wave packet focusing periods (thick lines) and from each run (thin lines) at high wind speed. The long wave case ($f_m = 1.0$ Hz) is shown in red and short wave case ($f_m = 1.0$ Hz) in blue. (c and d) Show log-log plots of the droplet diameter size distributions normalized by the number of recorded frames, measurement volume, and bin width. Weak, moderate, and strong wind speeds for the (c) long and (d) short wave cases. The vertical dashed line shows the minimum accepted droplet diameter $d_{min} = 38$ µm. The solid black lines indicate $N(d) \propto d^{-1}$ and $N(d) \propto d^{-4}$.

at 20 Hz. The measured values of U_0 range between 9.0 and 11.4 m/s for the experiments presented in this paper. The velocity profile in the air above the breaking waves is expected to resemble a modified channel flow and the flow close to the water surface is expected to be qualitatively similar to that of (Buckley et al., 2020), who measured the air flow using PIV in the same facility at similar wind speed conditions without any mechanical forcing. They found that the near surface mean velocity profiles conform to classical log-linear turbulent boundary profiles, albeit with modifications of the roughness length from the wind waves. In our experiments, droplets are not expected to interact with the part of the flow near the ceiling during their lifetime and the boundary layer is stable. Wave height was measured at a fetch of 22.9 m using a modified wave gauge (Akamina, Model: AWP -24-3) recording at 20 Hz. Weak, moderate, and strong wind speeds were tested for each forcing frequency and two to six 20-min runs are performed depending on the condition (see Supporting Information S1 for details). The wave amplitude a and peak frequency f_p are measured from the wave gauge data, with $a = \sqrt{2}a_{rms}$, where a_{rms} is the root mean square of the wave amplitude. Following the linear wave theory, k is calculated using the dispersion relation $\omega^2 = gk\tanh(kh)$, where $h = 0.71$ m is the mean water depth. The angular frequency is $\omega = 2\pi f_p$ and the phase speed, c_p, is $c_p = \omega/k$. See Supporting Information S1 for examples of wave height and spectrum measurements. The parametric space covered by the experiments is reported in terms of the wave slope, ak, and the ratio of the wind speed and wave phase speed, U_0/c_p. For the $f_m = 1.0$ Hz mechanical forcing, $ak = 0.15$–0.19 and $U_0/c_p = 5.9$–7.1, which results in long relatively fast moving waves and is referred to as the long wave case in this paper. In the $f_m = 1.8$ Hz case, $ak = 0.27$–0.33 and $U_0/c_p = 9.4$–11.1, which results in short waves with larger wave slopes which feel the influence of the wind for a larger area. These waves are referred to as the short waves in this paper.

Droplets are measured at a fetch of 23.3 m and 6.3 cm above the mean water level using a cinematic in-line holography system; see Katz and Sheng (2010) for details on the measurement technique. The holographic setup and processing method is similar to the one described in Erinin et al. (2019) and Néel et al. (2022). The illumination source is provided by a pulsed Nd:YLF laser (Model: QL527-200-L, CrystalLaser) and the holographic system is deployed in two configurations. In each configuration, the camera is fitted with a long-distance microscope

lens (K2 DistaMax, Infinity Photo-Optical Co.) which is focused close to the center of the tank. Fairing devices are installed on the walls of the tank near the camera field of view in order to prevent droplets from being deposited on the walls and obscuring the field of view of the cameras. Droplets are measured down to the minimum accepted droplet diameter, d_{min}, across the full tank width minus the width of the fairing devices (0.895 m). More details on the holographic system calibration and image processing are provided in Supporting Information S1. The first experimental configuration is a high-resolution setup which is used to obtain statistical droplet data such as number and diameter and utilizes a Phantom VEO4K-990-L at a frame rate of 100 Hz. The system has a spatial resolution of 4.7 μm/pixel with a field of view of 1.93×1.09 cm^2 (and a measurement volume of 188 cm^3). The minimum accepted droplet diameter measurement, corresponding to a droplet with diameter of 8 pixels, is $d_{min} = 38$ μm. Using the high resolution data the droplet number is measured as a function of diameter, and time, $N(d, t)$. The second experimental configuration is a high-speed setup which is used to obtain droplet trajectories. Holograms are recorded using a Phantom v2012 at a frame rate of 4,000 Hz with a spatial resolution of 20.15 μm/pixel, a field of view of 2.58×1.61 cm^2 (and a measurement volume of 371 cm^3), and $d_{min} = 161$ μm. Movie S1 shows an example of the droplet tracking at high speed during a time interval when many drops are detected. Droplet speeds and accelerations are measured from the trajectories; see Supporting Information S1 for more details. Using the high-speed setup the droplet number is measured as a function of diameter, horizontal and vertical velocities and accelerations, u, w, a_x, and a_z, respectively, and time, $N(d, u, w, a_x, a_z, t)$. Changes of droplet diameters for droplets with $d \geq 161$ μm are not measured since the typical droplet trajectory is measured for ≈2 ms by the holographic system. However, it is possible that droplets might have evaporated from the time they are ejected and while being transported to the measurement region, even if we expect this effect to be small, given the high relative humidity in the wave tank, which varied between 80% and 95% from run to run. In Section 4, droplet speed and acceleration PDFs are presented for three different ranges of droplet diameters (160 ≤ d ≤ 240 μm), (350 ≤ d ≤ 500 μm), and (600 ≤ d ≤ 1000 μm), referred to as small, moderate, and large droplet sizes, respectively. In order to show the relative difference between the three droplet sizes, their Kolmogorov-based Stokes number, St_η, based on the particle response time divided by the Kolmogorov time scale is estimated as $St_\eta \approx 58$, 142, and 263, respectively; see Supporting Information S1 for calculation details. These droplets are highly inertial and are comparable to the higher St_η cases in Berk and Coletti (2020), who report the vertical concentrations of inertial particles in a turbulent boundary layer for $St_\eta = 0.8$–230.

3. Wave Field and Droplet Characteristics

3.1. Wave Field Dynamics and Time Evolution of Droplet Population

We start by discussing the qualitative differences between the short ($f_m = 1.8$ Hz) and long ($f_m = 1.0$ Hz) waves and discuss them in the context of droplet number time-evolution, $N(t)$, and the wave field white light movies in Movies S2 and S3. In the short wave configuration, we observe nearly constant air entrainment and droplet ejection at most times a wave crest passes by; while, in the long wave configuration, fewer more energetic events are observed, typically one to two over a 20 s period.

The time-evolution of droplet production is found to be nearly constant in the short wave case and periodic in the long wave case. The thin solid line in Figure 1b shows $\overline{N}(t)$ from multiple 20 s wave packet focusing periods for the long and short wave cases at high wind speed while the thick solid lines show the ensemble averages. The droplet data is phase-aligned so that the maximum number of droplets produced in each 20 s period occurs at $t = 17.5$ s. In the long wave case, a pronounced absolute maximum many standard deviations greater than the mean signal is measured at $t = 17.5$ s. The absolute maxima is preceded by three local maxima occurring at regular intervals of ≈2.3 s. The average concentration of droplets is ≈1.4 droplets/image but locally in time, as many as 100 droplets can be observed in a single image. This suggests that drops are produced by regularly occurring energetic breaking events with few drops produced in-between. These observations are consistent with the qualitative observations from the white-light movies and those reported by Wu et al. (1984) in field measurements of droplets where they observed longitudinal patches of droplet concentrations that correlated with the dominant frequency of the wave field. In the short wave case, the absolute maxima is greatly diminished and no other pronounced local maxima are measured. This indicates that for the short wave case droplets are produced at a near continuous rate with an average concentration of approximately 20 droplets/image.
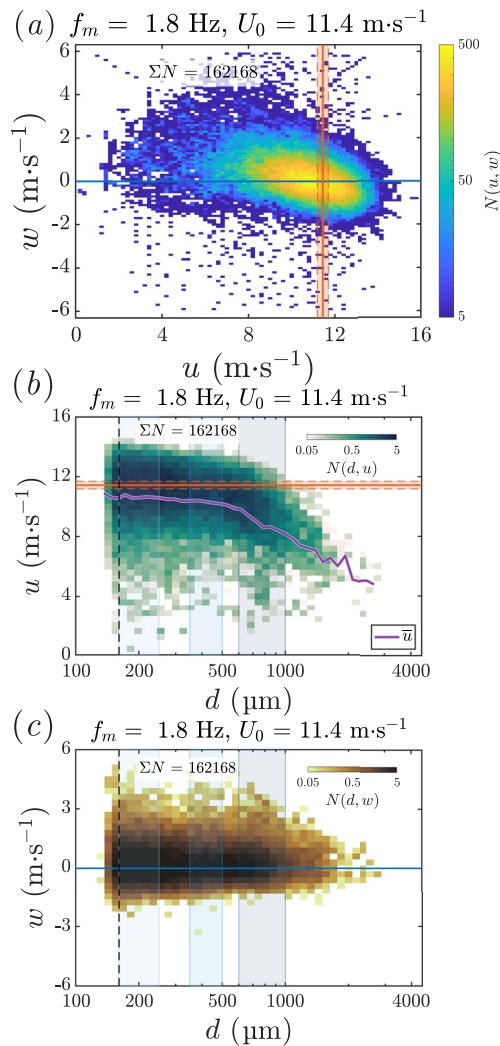
Figure 2. (a) Shows $N(u, w)$ per run per s per m^3 for the strong wind short wave case. The experimentally measured function, $N(u, w)$, is divided by the bin area, the number of recorded images in one run, number of runs, recording duration, and measurement volume. (b and c) Show the $N(u, d)$ and $N(w, d)$ per run per s per m^3 at high wind speed for the same wave case as panel (a). The black vertical dashed lines shows the minimum accepted droplet diameter, $d_{\min} = 161$ µm. The solid and dashed orange lines in panels (a and b) shows the average and ± 1 std of U_0 measured from the pitot tube. The blue rectangles in panels (b and c) show the three droplet diameter bin ranges used to calculate the u and w speed probability density functions shown in Figure 3. The purple line in panel (b) shows the average horizontal velocity, $\overline{u}$, calculated in each diameter bin.

3.2. Droplet Diameter Distributions

The total number of measured drops is found to increase with wind speed for the long and short wave cases. Figures 1c and 1d show the droplet diameter distributions, $N(d)$, the number of droplets per unit volume, which is obtained by integrating $N(d, t)$ from the high-resolution droplet data for the long and short wave cases, respectively. In the short wave cases, the number of droplets increases monotonically with wind speed. In contrast, in the long wave cases, the number of droplets produced between the weak and moderate wind speed is almost the same, while a larger increase is observed for the highest wind speed. This corresponds to more intermittent and intense breaking events in the long wave case, while the short wave case has more frequent and less intense breaking events. The effect may be related to the smaller wave slopes and lower U_0/c_p of the long wave cases, meaning the wind induces less momentum in the wave field, causing the wind to have an indirect influence on the breaking process.

The droplet size distributions feature two power law regions, one for large and one for small droplets, with a break in slope qualitatively observed around $d = 600$–700 µm. The data can be described by $N(d) \propto d^{-1}$ for the small droplets and $N(d) \propto d^{-4}$ for the large droplets. A similar break in slope has been observed in field and laboratory experiments (Erinin et al., 2019; Veron et al., 2012; Wu et al., 1984) with slightly steeper slopes.

4. Droplet Dynamics—Speeds and Accelerations

4.1. Droplet Velocity Distributions

The speed and acceleration time history of a droplet generated by a breaking wind wave is the result of complex interactions between the processes that produced the droplet from the bulk, the droplet inertia, and the interaction with the boundary layer, which is coupled to the wave field. We first discuss the time-integrated function $N(d, u, w)$ and analyze it by integration in d, w, and u resulting in $N(u, w)$, $N(d, u)$, and $N(d, w)$, respectively. Then, we consider three representative diameter bin ranges and construct PDFs of droplet speed, PDF(u) and PDF(w).

Figure 2a shows the joint speed distribution, $N(u, w)$, for the short wave case at high wind speed. The figure indicates that droplets with low horizontal speeds are more likely to travel upward and droplets with high horizontal speeds are more likely to travel downward. The slower horizontal speed of upward moving droplets could be explained by the fact that these droplets were recently generated, with their speed still influenced by the ejected mechanisms. These drops have not yet reached the horizontal free-stream speed. On the other end, droplets that have reached the free stream velocity (and have forgotten their initial ejection speed) have been traveling longer and are more likely to start falling down due to gravity. Additionally, the range of speeds observed for droplets moving up is about twice as large as the range of speeds for downward moving droplets. The large range of speeds for upward moving drops is likely related to a variability in the initial ejection velocity and the lower range in downward speed may be because these drops are closer to reaching terminal velocity. A similar u-w correlation is observed at for the long wave case, at lower wind speeds, and for different diameter bin droplets, see Supporting Information S1 for additional figures. These results are consistent with observations from Boulesteinx (2010) (see Figure V.20), who studied the dynamics of droplets in a pipe flow.

The droplet diameter-speed distributions, $N(d, u)$ and $N(d, w)$, are shown in Figures 2b and 2c, respectively, for the short wave case at high wind speed. The transparent vertical blue rectangles in Figures 2b and 2c show the
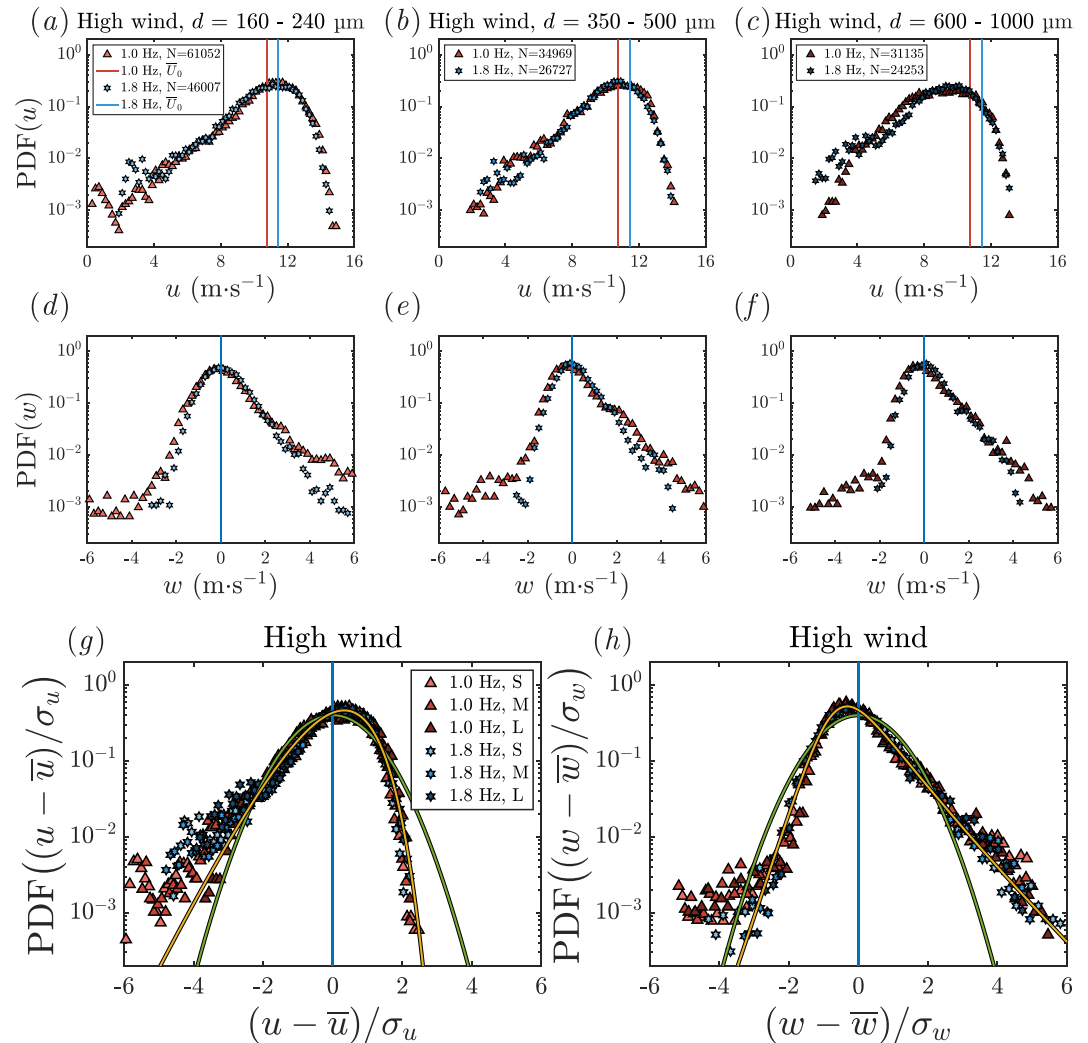
Figure 3. (a–c) Show the PDF(u) and (d–f) show the PDF(w) for small ($150 \leq d \leq 250$ µm) in panels (d and g), moderate ($350 \leq d \leq 500$ µm) in panels (e and h), and large ($600 \leq d \leq 1000$ µm) sized droplets for the long (in red) and short (in blue) wave conditions. The solid lines in panels (a–c) show the horizontal speed distributions measured from the pitot tube for the long (in red) and short (in blue) wave conditions at high wind speeds. Horizontal velocity droplet PDF $\left(\left(u - \overline{u}\right)/\sigma_u\right)$ is shown in panel (g) and vertical velocity drop size PDF $\left(\left(w - \overline{w}\right)/\sigma_w\right)$ in panel (h). The S/M/L labels in the legend refer to the small, moderate, and large drop diameter bins described above. The solid green lines in panels (g–h) shows a normalized Gaussian distribution. The solid yellow line in panels (g–h) shows a normal-inverse-Gaussian distribution described in Barndorff-Nielsen (1997) as suggested by Boulesteinx (2010); see text and Supporting Information S1 for fitting details.

droplet diameter ranges used to calculate the velocity PDFs in Figures 3a–3f. The measured function $N(d, u)$ has a downward oriented tail that becomes more pronounced for larger droplets, indicating larger droplets are more likely to have a slower horizontal velocity. $N(d, u)$ has a broad range of velocities from $u = 15$–4 m/s and extends out to $d = 1800$ µm, over 40 times greater than the standard deviation of U_0 ($\sigma_{U_0} = 0.255$ m/s). A significant number of small droplets have speeds greater than U_0 despite the fact that droplets are measured 6.3 cm above the mean water level, and U_0 is measured 36 cm above the mean water level. Using velocity profile measurements from Buckley et al. (2020), which were conducted with wind only forcing, the velocity at the measurement window is estimated to be approximately 8 m/s. The function $N(d, w)$ also has a wide distribution of droplets ranging from $w = -3$–6 m/s, skewed toward positive upward velocity, which is attributed to the ejection mechanisms. Approximately half of measured droplets have a positive w velocity. The average droplet vertical velocity in each radius bin is near zero for weak, moderate, and strong wind speeds for both short and long wave cases (see

Supporting Information S1 for additional figures). As wind speed increases, the size and speed range of $N(d, u)$ and $N(d, w)$ also increases.

The normalized PDF of u and w are found to be skewed normal in both direction. The distributions are calculated from the $N(d, u)$ and $N(d, w)$ for small ($150 \leq d \leq 250$ μm), moderate ($350 \leq d \leq 500$ μm), and large ($600 \leq d \leq 1000$ μm) droplets and is shown in Figures 3a–3f. Each figure shows data from the long and short wave cases at high wind speed and the total number of droplets comprising each u–w distribution pair is shown in the legend of the PDF(u) subplots. PDFs at moderate and weak wind speed conditions are shown in Supporting Information S1. Figures 3a–3c shows PDF(u), indicated by the markers. The solid lines show the mean pitot tube velocities for each respective wave condition. The three measured PDF(u) have asymmetric tails that extend out to low velocity with stronger asymmetry as droplet size increases. This asymmetry may be related to the role of drag and turbulence, which can accelerate the drop speed above the mean wind speed, while ejection speeds are mostly lower than the mean wind speed, so that overall finding a slower drop than the wind is more likely. The standard deviation of PDF(u) ranges from 2 to 4 m/s, 5–10 times greater than the standard deviation of U_0. A large number of droplets with speeds greater than U_0 are measured for small, moderate, and large droplet sizes. This result indicates that droplet motions may be influenced by the boundary layer significantly. The PDF(w), shown in Figures 3d–3f for small, moderate, and large droplets sizes, respectively, are also asymmetric. The vertical PDF distribution is skewed for all three droplet size ranges and the skew becomes more pronounced as droplet size increases. The positive tail in w extends to approximately $w = 6$ m/s and indicates that upward moving droplets have a larger range of speed than downward moving droplets, consistent with the discussion from Figure 2a. The fast upward traveling drops can be attributed to drops having been recently ejected. The shape and skewness of the horizontal and vertical velocity distributions are qualitatively similar to the ones shown in Boulesteinx (2010); see Figures V.21 and V.23 of that dissertation.

In order to analyze the features of the velocity distributions, the mean, variance, and skewness verses droplet diameter were computed and plotted; see Supporting Information S1 for figures. At small drop sizes $\bar{u} \approx U_0$ and decreases at a rate of approximately -0.2 m/s per 100 μm and after $d \geq 800$ μm about -0.3 m/s per 100 μm. The moments σ_u, skew(u), $\overline{w}$, σ_w, and skew(w) are shown in Supporting Information S1.

Figures 3g and 3h show PDF$\left(\left(u - \bar{u}\right)/\sigma_u\right)$ and PDF$\left(\left(w - \overline{w}\right)/\sigma_w\right)$ for small, moderate, and large droplets (denoted as S, M, and L in the legend, respectively) at high wind speed. All distributions are relatively well collapsed, suggesting that the knowledge of the mean and standard deviation speed at a specific size is enough to describe a universal droplet statistics close to the water surface. The normalized horizontal velocity distributions, shown in (g), have qualitatively similar shapes for all three droplet sizes. The horizontal velocity is asymmetric with an extended tail for low drop speeds and distributions becoming flared out at the extremes as droplet diameter decreases. The vertical velocity PDFs, shown in (h), are also asymmetric, with high upward velocities, which we attribute to the fast upward ejection velocities. The solid green curves show normalized Gaussian distributions and do not represent the asymmetry in the data. This can be interpreted as the velocity statistics being the result of the superposition of the distribution of ejection speeds (which mostly control the tail of high vertical velocity and low horizontal velocity), turbulent transport (which control values around the horizontal free stream velocities), and sedimentation (controlling negative vertical velocities). The skewness of the data in (g) and (h) is well

represented by a normal-inverse-Gaussian distribution (yellow line) (Barndorff-Nielsen, 1997), as suggested by Boulesteinx (2010). The PDF of the distribution has the form $P_{NIG}(\mathcal{U}) = \frac{\alpha \delta K_1 \left(\alpha \sqrt{\delta^2 + (\mathcal{U} - \mu)^2} \right)}{\pi \sqrt{\delta^2 + (\mathcal{U} - \mu)^2}} e^{\delta \sqrt{\alpha^2 - \beta^2} + \beta(\mathcal{U} - \mu)}$, where K_1 is a Bessel function of a second kind with index 1, and α, β, δ, and μ are fitting parameters (see Supporting Information S1 for more details and values). We note that two of the distribution parameters are constrained by the mean and standard deviation in this normalized representation, where $\mathcal{U}$ is the normalized velocity $\left(u - \bar{u}\right)/\sigma_u$ or $\left(w - \overline{w}\right)/\sigma_w$. The quality of the fits suggests that the normal-inverse-Gaussian distribution could universally represent the droplet velocity statistics close to the wave breaking surface. The speed PDFs, $S = \sqrt{u^2 + w^2}$, are shown in Supporting Information S1.
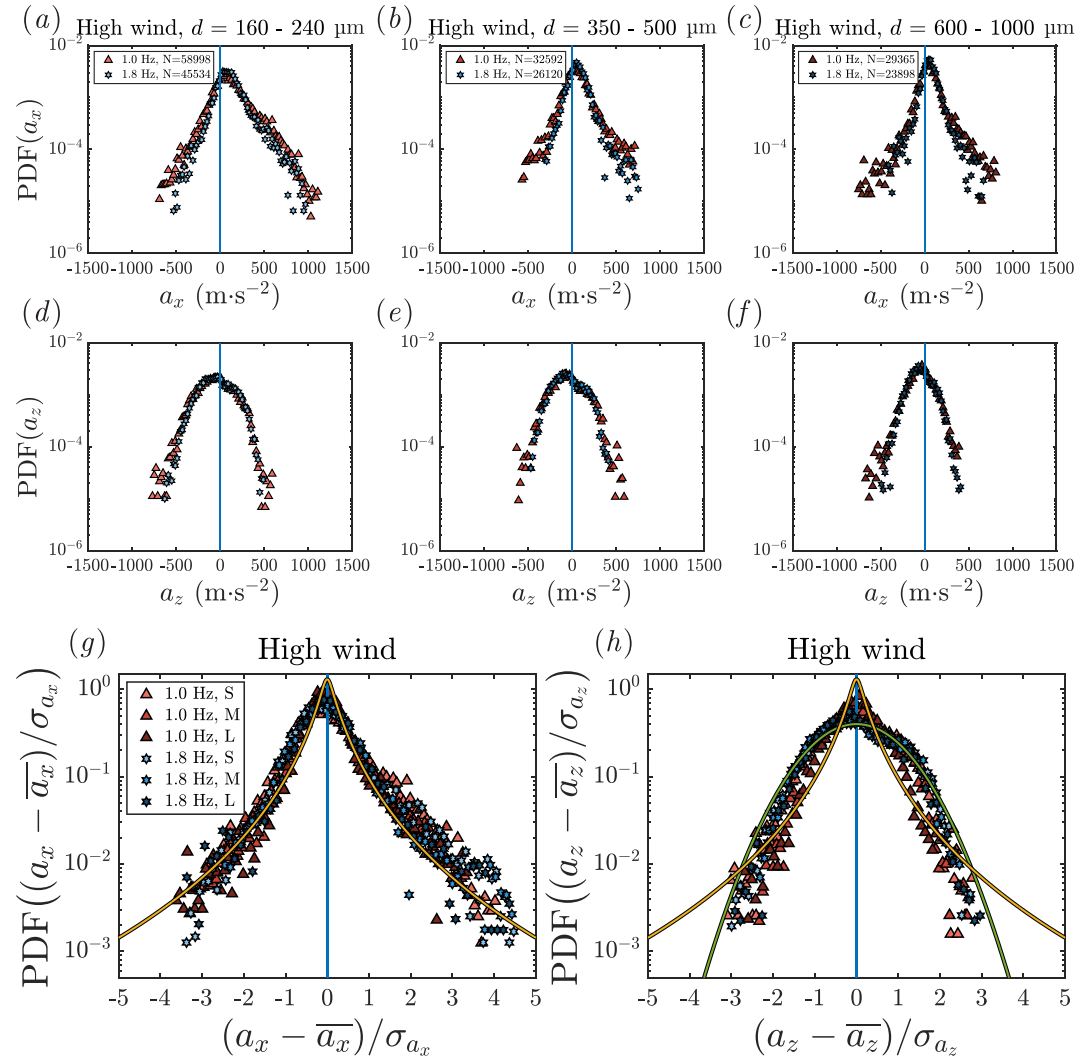
Figure 4. (a–f) Show the probability density functions (PDFs) of accelerations in the horizontal direction, a_x, in panels (a–c), and vertical direction, a_z, in panels (d–f), directions for small, moderate, and large droplets, using the same diameter bins as the data presented in Figure 2. The normalized PDFs, PDF $\left(\left(a_x - \overline{a_x} \right) / \sigma_{a_x} \right)$ and PDF $\left(\left(a_z - \overline{a_z} \right) / \sigma_{a_z} \right)$, are shown in panels (g and h), respectively. The solid yellow line in panels (g and h) is a comparison with a functional shape of the acceleration PDF proposed by Mordant et al. (2004) from homogeneous isotropic turbulence experiments. The green line in panel (h) is a normalized Gaussian distribution.

4.2. Droplet Acceleration Distributions

We present the droplet acceleration PDF in the horizontal (x) and vertical directions (z). Figures 4a–4c show the a_x acceleration PDFs and (d–f) show PDF(a_z) with the same small, moderate, and large diameter bins used above. Acceleration versus diameter joint distributions, $N(d, a_x)$ and $N(d, a_z)$, and the acceleration joint distributions, $N(a_x, a_z)$, are shown in Supporting Information S1. The magnitude of the reported accelerations is consistent with previous experimental studies, obtained in various configurations of turbulent air flow, see La Porta et al. (2001); Mordant et al. (2004); Stelzenmuller et al. (2017).

The horizontal acceleration distributions, PDF(a_x), are shown in (a–c). They feature a stretched exponential shape with long tails and pointed peaks. To the best of our knowledge, there is very limited data on acceleration statistics from droplets generated by breaking waves with Ramirez de la Torre et al. (2022) reporting acceleration measurements in wind speeds up to 5 m/s for fairly large drops. Many previous papers have focused on studying the acceleration of inertial and passive particles both experimentally and numerically in homogeneous isotropic turbulence (henceforth referred to as HIT) and boundary layers; see for example, La Porta et al. (2001);

Mordant et al. (2004); Bec et al. (2006); Stelzenmuller et al. (2017). The particle acceleration PDFs reported in these papers are qualitatively similar to the droplet accelerations in Figures 4a–4c. The shapes of the curves in Figures 4a–4c also feature an asymmetry toward positive acceleration, which becomes less pronounced for larger droplets. Indeed, drops are being ejected at a speed lower than the free stream velocity, so that they are accelerated by the turbulent boundary layer. This asymmetry in the acceleration PDF has been observed near the wall in experimental and numerical simulation of droplet acceleration in canonical boundary layer configurations; see Stelzenmuller et al. (2017) and Gerashchenko et al. (2008) and is attributed to the turbulence anisotropy near the wall. Similarities in the acceleration PDF with the canonical boundary layer is observed despite the effects of the moving wave boundary on the turbulent boundary layer.

The shape of the vertical droplet acceleration, $PDF(a_z)$, shown in (d–f), is very different from the horizontal acceleration and resembles a normal distribution shape. As droplet size increases, the distribution near the peak becomes sharper. This shape resembles the top portion of the distributions in (a–c) without the extended tails and has not been observed in previous studies of droplet acceleration in turbulent boundary layers Stelzenmuller et al. (2017). Despite the different mechanical wave forcing, the droplet acceleration distributions look very similar for each case, likely suggesting that the acceleration is primarily influenced by ejection mechanisms that generated the droplets. The moments of the distributions as a function of diameter of the acceleration distributions are shown in Supporting Information S1.

The solid yellow line in (g) is the acceleration PDF assuming a log-normal acceleration magnitude distribution and isotropic acceleration vector given by Equation 3 in Mordant et al. (2004): $P(a_i) = \frac{\exp(s^2/2)}{4m} \left[1 - \text{erf}\left(\frac{\ln\left(\frac{|a_i|}{m}\right) + s^2}{\sqrt{2}s} \right) \right]$.

In our plot, we use $m = \sqrt{3/e^{2s^2}}$ for a variance of 1 and $s = 1$, the same values used in Mordant et al. (2004) and Stelzenmuller et al. (2017). This model, which has been derived for tracer particles in HIT, describes the horizontal droplet acceleration PDF well and suggest that droplet acceleration statistics in the horizontal direction are controlled by the turbulence. The acceleration PDFs in the vertical direction are not well described by Equation 3 from Mordant et al. (2004), shown in yellow in (h). Instead, their shape looks similar to a normal distribution, shown by the green line in (h). The shape of the acceleration data is slightly skewed but qualitatively agrees with the normal distribution.

5. Concluding Remarks

We have presented measurements of droplet size, velocity, and acceleration distributions resulting from a breaking wind wave in a large-scale facility, down to 30 μm, for a range of wave slope (0.15–0.35) and ratio of wave speed over wind speed (5.9–11.1). A difference is observed between the long and short wave cases, where in the long wave case breaking events occur at regular intervals and are accompanied by an increase in detected droplets. In contrast, in the short wave case, droplets are produced at a near constant rate and individual breaking events are harder to identify. We observe that the size distribution can be described by $N(d) \propto d^{-1}$ for $d < 600$ μm and $N(d) \propto d^{-4}$ for $d > 600$ μm. The velocity and acceleration distribution are influenced by both the turbulent boundary layer, which is dynamically evolving and dependent on the wave state, and the generation processes. Droplet speeds are shown to have a $u - w$ dependency where drops with slow horizontal velocities are more likely to have a faster upward motion. We attribute these fast upward traveling drops to drops being freshly generated, which have not yet reached the free-stream velocity in the horizontal direction. A significant number of droplets are found to be going faster than the measured wind speed in the channel, which indicates that the turbulence in the boundary layer impacts drop motion. The droplet velocity PDFs are asymmetric and are well described by a normal-inverse-Gaussian distribution, which can be interpreted as the superposition of the effect of ejection speeds, turbulent transport, and sedimentation. The normalized acceleration PDFs in the horizontal and vertical directions are shown to have different shapes. The horizontal direction is found to have a distribution similar to the one observed in Mordant et al. (2004) for particles in homogeneous and isotropic turbulence. The vertical droplet accelerations more closely resemble Gaussian distributions. This data shed light on the velocity and acceleration statistics of drops generated by the breaking wind wave and can be used to inform spray transport and evaporation models.

Data Availability Statement

All data used in preparing this work are publicly available at https://doi.org/10.34770/s63n-xk73.

References

Aliseda, A., Cartellier, A., Hainaux, F., & Lasheras, J. C. (2002). Effect of preferential concentration on the settling velocity of heavy particles in homogeneous isotropic turbulence. *Journal of Fluid Mechanics*, *468*, 77–105. https://doi.org/10.1017/s0022112002001593

Andreas, E. L. (1992). Sea spray and the turbulent air-sea heat fluxes. *Journal of Geophysical Research*, *97*(C7), 11429–11441. https://doi.org/10.1029/92jc00876

Andreas, E. L., & Decosmo, J. (2002). The signature of sea spray in the HEXOS turbulent heat flux data. *Boundary-Layer Meteorology*, *103*(2), 303–333. https://doi.org/10.1023/a:1014564513650

Andreas, E. L., Jones, K. F., & Fairall, C. W. (2010). Production velocity of sea spray droplets. *Journal of Geophysical Research*, *115*(C12), C12065. https://doi.org/10.1029/2010jc006458

Barndorff-Nielsen, O. E. (1997). Processes of normal inverse Gaussian type. *Finance and Stochastics*, *2*(1), 41–68. https://doi.org/10.1007/s007800050032

Bec, J., Biferale, L., Boffetta, G., Celani, A., Cencini, M., Lanotte, A., et al. (2006). Acceleration statistics of heavy particles in turbulence. *Journal of Fluid Mechanics*, *550*, 349–358. https://doi.org/10.1017/s002211200500844x

Berk, T., & Coletti, F. (2020). Transport of inertial particles in high-Reynolds-number turbulent boundary layers. *Journal of Fluid Mechanics*, *903*, A18. https://doi.org/10.1017/jfm.2020.597

Boulesteinx, S. (2010). *Cisaillement d'une interface gaz-liquide en conduite et entraînement de gouttelettes [Shearing of a gas-liquid interface in a pipe and droplet entrainment]* (Doctoral dissertation). l'Université Paul Sabatier.

Brandt, L., & Coletti, F. (2022). Particle-laden turbulence: Progress and perspectives. *Annual Review of Fluid Mechanics*, *54*(1), 159–189. https://doi.org/10.1146/annurev-fluid-030121-021103

Bruch, W., Piazzola, J., Branger, H., van Eijk, A. M., Luneau, C., Bourras, D., & Tedeschi, G. (2021). Sea-spray-generation dependence on wind and wave combinations: A laboratory study. *Boundary-Layer Meteorology*, *180*(3), 477–505. https://doi.org/10.1007/s10546-021-00636-y

Buckley, M., Veron, F., & Yousefi, K. (2020). Surface viscous stress over wind-driven waves with intermittent airflow separation. *Journal of Fluid Mechanics*, *905*, A31. https://doi.org/10.1017/jfm.2020.760

Deike, L. (2022). Mass transfer at the ocean–atmosphere interface: The role of wave breaking, droplets, and bubbles. *Annual Review of Fluid Mechanics*, *54*(1), 191–224. https://doi.org/10.1146/annurev-fluid-030121-014132

De Leeuw, G. (1986). Vertical profiles of giant particles close above the sea surface. *Tellus B: Chemical and Physical Meteorology*, *38*(1), 51–61. https://doi.org/10.1111/j.1600-0889.1986.tb00087.x

De Leeuw, G., Andreas, E. L., Anguelova, M. D., Fairall, C., Lewis, E. R., O'Dowd, C., et al. (2011). Production flux of sea spray aerosol. *Reviews of Geophysics*, *49*(2), RG2001. https://doi.org/10.1029/2010rg000349

Erinin, M. A., Wang, S. D., Liu, R., Towle, D., Liu, X., & Duncan, J. H. (2019). Spray generation by a plunging breaker. *Geophysical Research Letters*, *46*(14), 8244–8251. https://doi.org/10.1029/2019gl082831

Fairall, C., Banner, M., Peirson, W., Asher, W., & Morison, R. (2009). Investigation of the physical scaling of sea spray spume droplet production. *Journal of Geophysical Research*, *114*(C10), C10001. https://doi.org/10.1029/2008jc004918

Gerashchenko, S., Sharp, N., Neuscamman, S., & Warhaft, Z. (2008). Lagrangian measurements of inertial particle accelerations in a turbulent boundary layer. *Journal of Fluid Mechanics*, *617*, 255–281. https://doi.org/10.1017/s0022112008004187

Huck, P. D., Bateson, C., Volk, R., Cartellier, A., Bourgoin, M., & Aliseda, A. (2018). The role of collective effects on settling velocity enhancement for inertial particles in turbulence. *Journal of Fluid Mechanics*, *846*, 1059–1075. https://doi.org/10.1017/jfm.2018.272

Ireland, P. J., Bragg, A. D., & Collins, L. R. (2016). The effect of Reynolds number on inertial particle dynamics in isotropic turbulence. Part 2. Simulations with gravitational effects. *Journal of Fluid Mechanics*, *796*, 659–711. https://doi.org/10.1017/jfm.2016.227

Katz, J., & Sheng, J. (2010). Applications of holography in fluid mechanics and particle dynamics. *Annual Review of Fluid Mechanics*, *42*(1), 531–555. https://doi.org/10.1146/annurev-fluid-121108-145508

Koga, M. (1981). Direct production of droplets from breaking wind-waves—Its observation by a multi-colored overlapping exposure photographing technique. *Tellus*, *33*(6), 552–563. https://doi.org/10.1111/j.2153-3490.1981.tb01781.x

Koga, M. (1984). Dispersal of droplets over breaking wind waves under the direct action of wind. *Journal of the Oceanographical Society of Japan*, *40*(1), 29–38. https://doi.org/10.1007/bf02071206

La Porta, A., Voth, G. A., Crawford, A. M., Alexander, J., & Bodenschatz, E. (2001). Fluid particle accelerations in fully developed turbulence. *Nature*, *409*(6823), 1017–1019. https://doi.org/10.1038/35059027

Laussac, S., Piazzola, J., Tedeschi, G., Yohia, C., Canepa, E., Rizza, U., & Van Eijk, A. (2018). Development of a fetch dependent sea-spray source function using aerosol concentration measurements in the North-Western Mediterranean. *Atmospheric Environment*, *193*, 177–189. https://doi.org/10.1016/j.atmosenv.2018.09.009

Lenain, L., & Melville, W. K. (2017). Evidence of sea-state dependence of aerosol concentration in the marine atmospheric boundary layer. *Journal of Physical Oceanography*, *47*(1), 69–84. https://doi.org/10.1175/jpo-d-16-0058.1

Mehta, S., Ortiz-Suslow, D. G., Smith, S., & Haus, B. (2019). A laboratory investigation of spume generation in high winds for fresh and seawater. *Journal of Geophysical Research: Atmospheres*, *124*(21), 11297–11312. https://doi.org/10.1029/2019jd030928

Mestayer, P., & Lefauconnier, C. (1988). Spray droplet generation, transport, and evaporation in a wind wave tunnel during the Humidity Exchange over the Sea Experiments in the Simulation Tunnel. *Journal of Geophysical Research*, *93*(C1), 572–586. https://doi.org/10.1029/jc093ic01p00572

Monahan, E. C. (1986). The ocean as a source for atmospheric particles. In *The role of air-sea exchange in geochemical cycling* (pp. 129–163). Springer.

Mora, D. O., Obligado, M., Aliseda, A., & Cartellier, A. (2021). Effect of Re_λ and Rouse numbers on the settling of inertial droplets in homogeneous isotropic turbulence. *Physical Review Fluids*, *6*(4), 044305. https://doi.org/10.1103/physrevfluids.6.044305

Mordant, N., Crawford, A. M., & Bodenschatz, E. (2004). Three-dimensional structure of the Lagrangian acceleration in turbulent flows. *Physical Review Letters*, *93*(21), 214501. https://doi.org/10.1103/physrevlett.93.214501

Mostert, W., Popinet, S., & Deike, L. (2022). High-resolution direct simulation of deep water breaking waves: Transition to turbulence, bubbles and droplets production. *Journal of Fluid Mechanics*, *942*, A27. https://doi.org/10.1017/jfm.2022.330

Mueller, J. A., & Veron, F. (2014a). Impact of sea spray on air–sea fluxes. Part i: Results from stochastic simulations of sea spray drops over the ocean. *Journal of Physical Oceanography*, *44*(11), 2817–2834. https://doi.org/10.1175/jpo-d-13-0245.1

Mueller, J. A., & Veron, F. (2014b). Impact of sea spray on air–sea fluxes. Part ii: Feedback effects. *Journal of Physical Oceanography*, *44*(11), 2835–2853. https://doi.org/10.1175/jpo-d-13-0246.1

Néel, B., Erinin, M., & Deike, L. (2022). Role of contamination in optimal droplet production by collective bubble bursting. *Geophysical Research Letters*, *49*(1), e2021GL096740. https://doi.org/10.1029/2021gl096740

Obligado, M., Cartellier, A., Aliseda, A., Calmant, T., & de Palma, N. (2020). Study on preferential concentration of inertial particles in homogeneous isotropic turbulence via Big-Data techniques. *Physical Review Fluids*, *5*(2), 024303. https://doi.org/10.1103/physrevfluids.5.024303

Ovadnevaite, J., Manders, A., De Leeuw, G., Ceburnis, D., Monahan, C., Partanen, A.-I., et al. (2014). A sea spray aerosol flux parameterization encapsulating wave state. *Atmospheric Chemistry and Physics*, *14*(4), 1837–1852. https://doi.org/10.5194/acp-14-1837-2014

Peng, T., & Richter, D. (2017). Influence of evaporating droplets in the turbulent marine atmospheric boundary layer. *Boundary-Layer Meteorology*, *165*(3), 497–518. https://doi.org/10.1007/s10546-017-0285-7

Pujara, N., Voth, G. A., & Variano, E. A. (2019). Scale-dependent alignment, tumbling and stretching of slender rods in isotropic turbulence. *Journal of Fluid Mechanics*, *860*, 465–486. https://doi.org/10.1017/jfm.2018.866

Ramirez de la Torre, R. G., Vollestad, P., & Jensen, A. (2022). Experimental investigation of droplet generation by post-breaking plunger waves. *Water Waves*, *4*(1), 1–21.

Reid, J. S., Jonsson, H. H., Smith, M. H., & Smirnov, A. (2001). Evolution of the vertical profile and flux of large sea-salt particles in a coastal zone. *Journal of Geophysical Research*, *106*(D11), 12039–12053. https://doi.org/10.1029/2000jd900848

Richter, D. H., Dempsey, A. E., & Sullivan, P. P. (2019). Turbulent transport of spray droplets in the vicinity of moving surface waves. *Journal of Physical Oceanography*, *49*(7), 1789–1807. https://doi.org/10.1175/jpo-d-19-0003.1

Smith, M., Park, P., & Consterdine, I. (1993). Marine aerosol concentrations and estimated fluxes over the sea. *Quarterly Journal of the Royal Meteorological Society*, *119*(512), 809–824. https://doi.org/10.1002/qj.49711951211

Sroka, S., & Emanuel, K. (2021). A review of parameterizations for enthalpy and momentum fluxes from sea spray in tropical cyclones. *Journal of Physical Oceanography*, *51*(10), 3053–3069. https://doi.org/10.1175/jpo-d-21-0023.1

Stelzenmuller, N., Polanco, J. I., Vignal, L., Vinkovic, I., & Mordant, N. (2017). Lagrangian acceleration statistics in a turbulent channel flow. *Physical Review Fluids*, *2*(5), 054602. https://doi.org/10.1103/physrevfluids.2.054602

Sumbekova, S., Cartellier, A., Aliseda, A., & Bourgoin, M. (2017). Preferential concentration of inertial sub-Kolmogorov particles: The roles of mass loading of particles, Stokes numbers, and Reynolds numbers. *Physical Review Fluids*, *2*(2), 024302. https://doi.org/10.1103/physrevfluids.2.024302

Tang, S., Yang, Z., Liu, C., Dong, Y.-H., & Shen, L. (2017). Numerical study on the generation and transport of spume droplets in wind over breaking waves. *Atmosphere*, *8*(12), 248. https://doi.org/10.3390/atmos8120248

Troitskaya, Y., Kandaurov, A., Ermakova, O., Kozlov, D., Sergeev, D., & Zilitinkevich, S. (2018). The "bag breakup" spume droplet generation mechanism at high winds. Part i: Spray generation function. *Journal of Physical Oceanography*, *48*(9), 2167–2188. https://doi.org/10.1175/jpo-d-17-0104.1

Variano, E. A., & Cowen, E. A. (2013). Turbulent transport of a high-Schmidt-number scalar near an air–water interface. *Journal of Fluid Mechanics*, *731*, 259–287. https://doi.org/10.1017/jfm.2013.273

Veron, F. (2015). Ocean spray. *Annual Review of Fluid Mechanics*, *47*(1), 507–538. https://doi.org/10.1146/annurev-fluid-010814-014651

Veron, F., Hopkins, C., Harrison, E., & Mueller, J. (2012). Sea spray spume droplet production in high wind speeds. *Geophysical Research Letters*, *39*(16), L16602. https://doi.org/10.1029/2012gl052603

Wang, Z., Yang, J., & Stern, F. (2016). High-fidelity simulations of bubble, droplet and spray formation in breaking waves. *Journal of Fluid Mechanics*, *792*, 307–327. https://doi.org/10.1017/jfm.2016.87

Wu, J., Murray, J. J., & Lai, R. J. (1984). Production and distributions of sea spray. *Journal of Geophysical Research*, *89*(C5), 8163–8169. https://doi.org/10.1029/jc089ic05p08163

References From the Supporting Information

Barndorff-Nielsen, O. E. (1997). Processes of normal inverse gaussian type. *Finance and Stochastics*, *2*(1), 41–68.

Buckley, M., Veron, F., & Yousefi, K. (2020). Surface viscous stress over wind-driven waves with intermittent airflow separation. *Journal of Fluid Mechanics*, 905.

Clift, R., Grace, J. R., & Weber, M. E. (2005). *Bubbles, drops, and particles*. Courier Corporation.

Erinin, M. A. (2020). *The dynamics of plunging breakers and the generation of spray droplets* (Unpublished doctoral dissertation). University of Maryland, College Park.

Erinin, M. A., Wang, S. D., Liu, R., Towle, D., Liu, X., & Duncan, J. H. (2019). Spray generation by a plunging breaker. *Geophysical Research Letters*, *46*(14), 8244–8251.

Guildenbecher, D. R., Gao, J., Reu, P. L., & Chen, J. (2013). Digital holography simulations and experiments to quantify the accuracy of 3d particle location and 2d sizing using a proposed hybrid method. *Applied Optics*, *52*(16), 3790–3801.

Katz, J., & Sheng, J. (2010). Applications of holography in fluid mechanics and particle dynamics. *Annual Review of Fluid Mechanics*, *42*, 531–555.

Li, C., Miller, J., Wang, J., Koley, S., & Katz, J. (2017). Size distribution and dispersion of droplets generated by impingement of breaking waves on oil slicks. *Journal of Geophysical Research: Oceans*, *122*(10), 7938–7957.

Néel, B., Erinin, M., & Deike, L. (2022). Role of contamination in optimal droplet production by collective bubble bursting. *Geophysical Research Letters*, e2021GL096740.

Pope, S. B. (2000). *Turbulent flows*. Cambridge University Press.